PLANETARY SCIENCE

A source of very energetic oxygen located in Jupiter's inner radiation belts

Elias Roussos[1]*, Christina Cohen[2], Peter Kollmann[3], Marco Pinto[4], Norbert Krupp[1], Patricia Gonçalves[4], Konstantinos Dialynas[5]

Jupiter hosts the most hazardous radiation belts of our solar system that, besides electrons and protons, trap an undetermined mix of heavy ions. The details of this mix are critical to resolve because they can reveal the role of Jupiter's moons relative to other less explored energetic ion sources. Here, we show that with increasing energy and in the vicinity of Jupiter's moon Amalthea, the belts' ion composition transitions from sulfur- to oxygen-dominated due to a local source of ≳50 MeV/nucleon oxygen. Contrary to Earth's and Saturn's radiation belts, where their most energetic ions are supplied through atmospheric and ring interactions with externally accelerated cosmic rays, Jupiter's magnetosphere powers this oxygen source internally. The underlying source mechanism, involving either Jovian ring spallation by magnetospheric sulfur or stochastic oxygen heating by low-frequency plasma waves, puts Jupiter's ion radiation belt in the same league with that of astrophysical particle accelerators.

INTRODUCTION

Radiation belts are a major component of all large-scale magnetospheres of our solar system (*1*, *2*). They occupy the region near each planet where a strong dipole-like magnetic field can trap and accumulate high intensities of charged particles that are produced or accelerated to very high energies through a variety of processes (*3*). These processes and their synergies can differ substantially among the various planets, which is why the study of different radiation belt systems offers unique insights on the range of possibilities that exist for generating cosmic particle radiation in our solar system and beyond.

Among the five strongly magnetized planets in our solar system (Earth, Jupiter, Saturn, Uranus, and Neptune), Jupiter is host to the largest and most energetic radiation belts, trapping electrons and protons with energies in excess of 70 MeV and 1 GeV, respectively (*4*–*6*). Different from Earth and Saturn, the ion radiation belts of which are dominated by protons ($Z = 1$) and contain trace abundances of heavier ions up to oxygen ($2 \leq Z \leq 8$) (*7*–*10*), Jupiter's heavy ion radiation belt is composed of high fluxes of ions as heavy as oxygen, sodium, and sulfur ($Z \leq 16$) (*6*, *11*–*20*). This belt occupies a large fraction of the planet's magnetosphere, with its highest intensity region located inward of Europa's M-shell at $M \lesssim 9.5$ (the M-shell, M, is defined as the distance that a field line based on a Jovian magnetic field model crosses the magnetic equator, normalized to a planetary radius of 1 R_J = 71,492 km; see Materials and Methods, subsection "M-shell and pitch angle estimates"). Sulfur and oxygen are the belt's most abundant heavy ions, dominating at least up to 50 MeV/nucleon for $M > 4.5$. The existence of these two species has been linked to Io's volcanic activity and to the sputtering of Europa's surface, but neither their acceleration pathway is fully resolved nor the action of additional non–moon-related energetic particle sources has been excluded. Inward adiabatic transport from a distant magnetospheric source contributes, at least in part, to the energization of oxygen and sulfur down to $M = 4.5$ (*14*, *16*, *18*).

In the heart of the heavy ion radiation belt ($M < 4.5$), the situation is less clear, especially for ion energies above 10 MeV/nucleon. Measurements from Pioneer 11, the Galileo Probe, and Juno show that ≫10 MeV/nucleon ions have several large intensity peaks and dropouts in their radial distribution. The dropouts are located at the M-shells of Jupiter's main ring at $M \sim 2$ and at the Jovian moons Amalthea and Thebe, at $M \sim 2.6$ and $M \sim 3.1$, respectively. The energy distribution of the heavy ions, which comprises an undetermined mix of species like helium, carbon, oxygen, and sulfur, extends well above 100 MeV/nucleon. These observations are difficult to reconcile by invoking energetic ion source mechanisms that explain the presence of the most energetic protons or heavier ions at Earth and Saturn. The cosmic ray albedo neutron decay (CRAND), a process where secondary neutrons from galactic cosmic ray (GCR) collisions with planetary atmospheres or rings β-decay into trapped magnetospheric charged particles (*8*, *21*), may only generate protons and electrons. The presence of very energetic heavy ions at Earth has been linked to the capture of anomalous cosmic rays (ACRs) through their charge stripping in our planet's atmosphere (*22*), but this mechanism has been convincingly rejected for Jupiter (*20*) because ACRs do not have enough energy to reach its atmosphere at latitudes mapping to $M < 4.5$.

Alternative theories that may explain the presence of very energetic heavy ions in Jupiter's inner radiation belts involve the adiabatic inward transport of oxygen and sulfur, which have been resolved at <50 MeV/nucleon and $M > 4.5$ as mentioned earlier, or the direct release of energetic heavy ions through spallation reactions between Jovian ring grains and trapped relativistic protons (*13*, *16*, *23*). The lack of observations that constrain the composition and the distribution function of heavy ions in the inner radiation belts, however, precludes any conclusion on the validity of the aforementioned theories.

In this work, we address these open issues through the analysis of energetic heavy ion observations from Jupiter's radiation belts that were obtained during the periapses of the first and the two last orbits of the Galileo spacecraft around Jupiter, namely, orbit J0 (day 341/1995 15:30 to 23:44), A34 (day 308/2002 21:48 to day 309/2002 06:35),

[1]Max Planck Institute for Solar System Research, Goettingen, Germany. [2]Space Radiation Lab, California Institute of Technology, Pasadena, CA, USA. [3]Johns Hopkins Applied Physics Laboratory, Laurel, MD, USA. [4]Laboratory of Instrumentation and Experimental Particle Physics, Lisbon, Portugal. [5]Office of Space Research and Technology, Academy of Athens, Athens, Greece.
*Corresponding author. Email: roussos@mps.mpg.de

and J35 (day 264/2003 06:58 to 18:15). During these periapses, the only ones of the mission reaching considerably deeper than Io's M-shell ($M \sim 5.9$), Galileo collected measurements down to $M \sim 2.2$. The data that we analyze originate primarily from Galileo's heavy ion counter (HIC) (*24*), occasionally complemented by observations from the composition measurement system of the energetic particle detector (EPD/CMS) (*25*). Both instruments contain solid-state detector (SSD) stacks that allow to resolve the composition, the energy spectra, and the angular distribution of heavy ions ($Z \geq 4$ for HIC and $Z \geq 2$ for EPD/CMS), together covering an energy range starting from 0.1 MeV/nucleon and reaching above 100 MeV/nucleon (see Materials and Methods, subsection "Instrumentation and datasets").

OBSERVATIONS

M-shell distribution and long-term temporal variations of energetic heavy ions

Figure 1 shows the M-shell profiles of heavy ion count rates recorded in four HIC energy ranges (>5 MeV/nucleon) during the three aforementioned Galileo periapses. The different spread of the count rates is a feature of the varying time resolutions of the raw measurements. Although the comparison between the three orbits, which are separated by about one or several years, shows that weak changes in the count rates of several HIC channels do occur, especially near or outside Io's M-shell, overall the heavy ion radiation belt profiles and intensities at $M \lesssim 6$ appear quasi-stable over long time scales. Further supporting this is that the M-shell profiles resemble those obtained by Pioneer 11, Voyager 1, and the Galileo Probe (*13*, *14*, *23*). For this reason, we focus on the continuous high–time resolution observations of orbit A34 (Fig. 1, black points), which we treat as representative of the steady-state configuration of the system. Unless otherwise stated, time variability will be considered a secondary effect.

All the M-shell profiles in Fig. 1 display significant count rate dropouts at Io, Thebe, and Amalthea, reminiscent of the proton radiation belts of Saturn, where its large moons efficiently sweep out megaelectronvolt protons from their M-shells (*26*–*28*). The moons in Saturn's radiation belts form impenetrable barriers to the radial transport of megaelectronvolt protons that lead to negligible proton intensities around their orbits (*21*). On the other hand, HIC measurements at Jupiter shown in Fig. 1 (A to C) indicate that the intensity of heavy ions is decreased, but it is not negligible near the moon orbits. A question arising from this observation is whether the heavy ions transmitted and heated adiabatically across the moon sweeping corridors are sufficient to account for the strong

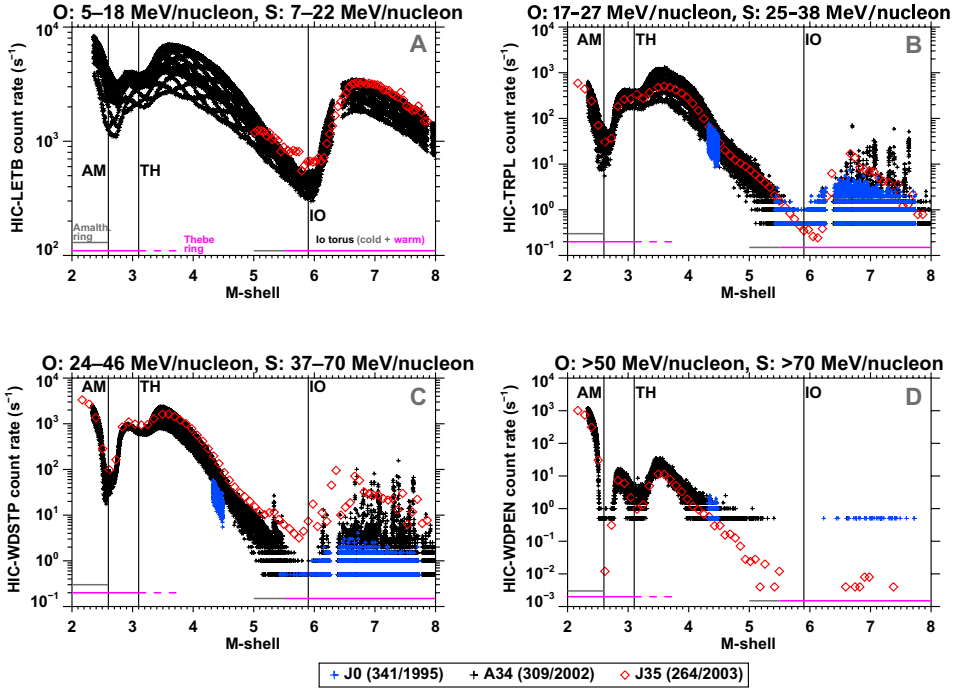

Fig. 1. M-shell distribution of energetic ion count rates. All panels show the M-shell distribution of heavy ion count rates at four energy ranges. The color coding of the data indicates different time periods. Measurements are obtained from four HIC channels, denoted as LETB, TRPL, WDSTP, and WDPEN, with their energy responses for oxygen and sulfur provided in the plot titles (see also figs. S1 and S2 and table S1 and the HIC description in Materials and Methods, subsection "Instrumentation and datasets"). The approximate M-shells of Amalthea (AM), Thebe (TH), and Io (IO); the Amalthea and Thebe rings; and the cold and warm components of the Io torus are marked. The Amalthea and Thebe rings are also commonly referred to as Jupiter's Gossamer rings. The dashed lines for the Thebe ring indicate its low-density, diffuse outer extension (*31*). All data are shown at their original time resolution. The minimum count rate threshold for high–time resolution measurements (**B** to **D**) corresponds to the single-count level with a sampling interval of 2 s. For orbit J35, the sampling interval was 4 min, explaining the much lower count rate threshold, especially in (D). In (**A**), measurements for orbit J35 inward of $M = 5$ are missing because the channel LETB malfunctioned, while for orbit J0, the corresponding measurements are not shown because of frequent calibration changes (*15*). The slightly lower rates at $M \sim 4.5$ in orbit J0, mostly visible in channel WDSTP (C), are due to the higher magnetic latitude of Galileo for that orbit compared to orbits A34 and J35. Data from a close Amalthea flyby on day 309/2003 (06:18:40 UTC) last less than a minute and occupy an M-shell range lower than 0.01 at $M \sim 2.58$. They are not resolved in the scale of these plots and do not affect our follow-up analysis.

signal measured in the innermost radiation belts, in particular, the two- to five-order-of-magnitude count rate increase inward of Amalthea developing over a $\delta M \sim 0.3$ (Fig. 1, B to D). To interpret all these signatures, in the following sections, we break down the M-shell profiles shown in Fig. 1, which mix contributions from multiple species, pitch angles and energies, to their different components.

Heavy ion composition

Ion composition can include key signatures on the ion source and acceleration processes. Naively, one might expect an O/S ratio of two, assuming that all ions are sourced from SO_2 released by Io. A larger O contribution may indicate a significant role of H_2O from Europa or that lighter ions are more efficiently accelerated. The three panels of Fig. 2 display estimates of the energetic heavy ion composition inward of Io's M-shell during Galileo's A34 orbit, including samples of raw data based on which these estimates were derived. The left panels of Fig. 2 show that the coincident ionizing energy losses of heavy ions on different combinations of HIC's SSDs cluster around the energy loss regimes expected for oxygen and sulfur (see Materials and Methods, subsection "Instrumentation and datasets," and fig. S1).

Without distinguishing yet for energy or location, oxygen is overall more abundant than sulfur. On the basis of the HIC events clustering in the regime where species tracks are separated, oxygen and sulfur reach at least up to ~80 and ~100 MeV/nucleon, respectively. Above those energies, the characteristic energy loss tracks of ions fold back and overlap (Fig. 2B) such that relevant HIC events cannot be unambiguously assigned to a specific ion species. Still, the large number of lower energy oxygen events and the lack of any appreciable signal along the carbon track indicates that the denser event cloud in the regime where tracks overlap (LE3 energy loss < 100 MeV) is due to oxygen ions. By using the species tracks to convert these energy losses to ambient ion energies in the magnetosphere (see Materials and Methods, subsection "Processing of HIC measurements"), we estimate that radiation belt oxygen and sulfur reach at least up to ~300 and ~100 MeV/nucleon, respectively.

After selecting the oxygen and sulfur events (see fig. S3), we construct profiles of their ratio (O/S) for different M-shells and energies (Fig. 2C). The general trend of the O/S ratio is to increase with energy. This is valid even when we consider heavy ion observations below 7 MeV/nucleon and in the EPD/CMS energy range, which show that sulfur can be more abundant than oxygen (fig. S7). Toward 100 MeV/nucleon, oxygen becomes dominant, with typical values for O/S > 5. The ratio is quasi-constant between Io and Thebe, except for the 7 to 18 MeV/nucleon range where it reduces slightly toward Thebe. Inward of Thebe or Amalthea (depending on energy), O/S increases significantly. For $M < 2.5$, sulfur events are only observed up to ~30 MeV/nucleon, meaning that, for 30 to 100 MeV/nucleon, the ratio should greatly exceed the values observed at larger M-shells ($O/S \gg 10$). The increase is significant also for 7 to 18 MeV/nucleon ions. This indicates that there is a preferential acceleration or production of oxygen and/or strong sulfur losses at Amalthea and Jupiter's rings. By constructing the M-shell profiles of phase space density (PSD) for oxygen and sulfur, the case of a local oxygen source gains stronger support.

M-shell profiles of heavy ion phase space densities

PSD profiles at constant values of adiabatic invariants are the basis for quantitatively understanding the physical processes acting in a

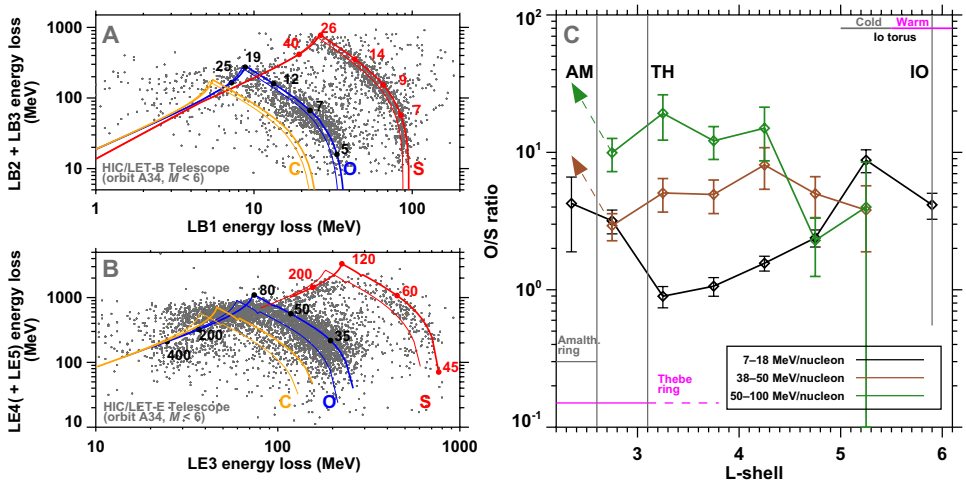

Fig. 2. Energetic ion composition inward the M-shell of Io ($M < 6$). (**A** and **B**) Pulse height analyzed (PHA) events from the two particle telescopes of HIC (LET-B and LET-E) for orbit A34. Each data point corresponds to coincident energetic ion energy losses on different SSDs of the telescopes, described in more detail in Materials and Methods (subsection "Instrumentation and datasets" and fig. S1). Orange, blue, and red curves mark the simulated tracks of carbon, oxygen, and sulfur, respectively. Thin lines are for normal ion incidence on the HIC SSDs, while the thick line is for the maximum incidence angle allowed through HIC's aperture. Clusters of O and S events spread beyond the area occupied by each pair of curves mostly due to random fluctuations of ion energy losses (straggling) (*60*). The numbering on each curve corresponds to oxygen's (black) and sulfur's (red) ambient kinetic energy in the magnetosphere in MeV/nucleon. (A) Double and triple coincidence events (channel LETB), with ions stopping at detector LB2 or LB3 of telescope LET-B. (B) Triple coincidence events, with ions stopping in SSD LE4 (channel WDSTP, $\delta E_{LE5} \sim 0$) or traversing LE4, leaving some energy in LE5 (channel WDPEN). Note that for channel WDPEN, HIC was storing the sum of LE4 + LE5 losses and did not downlink data from these two detectors separately. Figure S3 shows PHA events and species classification for all four channels of HIC, separated. (**C**) Evolution of the O/S ratio as a function of energy and M-shell. The energy ranges in Fig. 2C are chosen from regimes where HIC is equally sensitive in detecting oxygen and sulfur. For the highest energy range, sulfur events are absent inward of Amalthea. The arrows indicate that because of that, the O/S ratio should significantly increase compared to $M > 2.6$.

radiation belt. A key diagnostic is the profiles' M-shell gradient, with PSDs falling toward a planet (positive gradient) indicating a steady diffusive inward transport. Planetward rising PSDs (negative gradient) hint the presence of local sources. Figure 3 shows M-shell profiles of oxygen and sulfur PSDs at constant first adiabatic invariant (μ). Their derivation is described in Materials and Methods (subsection "Processing of HIC measurements"). A key step was the calculation of oxygen and sulfur differential flux spectra (fig. S6), using observations from both HIC and EPD/CMS.

For most μ ranges and between Io and Amalthea, we find PSD profiles with a positive or nearly zero M-shell gradient ($3.5 < M < 5.5$). A flattening of oxygen PSD profiles between Io and $M \sim 4.5$ has been reported also in an earlier study (*16*). Losses, evident in regions where positive PSD gradients become steeper, are seen for both species at Io's, Thebe's, and Amalthea's M-shells, as anticipated from observations shown in Fig. 1, fig. S6, and earlier works (*13*, *16*). These gradients become stronger with increasing μ (or energy) for a fixed M-shell.

A strong case of negative oxygen PSD gradient is observed inward of Amalthea: ~300 MeV/(G nucleon) PSDs increase sharply by nearly two orders of magnitude, with evidence that an increase is present also at lower μ. This suggests that a source is locally accelerating or producing very energetic oxygen. The minimum energy where this source is clearly resolved is at ~50 MeV/nucleon, but given the HIC energy resolution and uncertainties in flux and PSD determinations, this limit may go as low as 30 MeV/nucleon. Another notable increase of PSD toward Jupiter is seen for $\mu \geq 900$ MeV/(G nucleon), inward of Io's M-shell, but relevant uncertainties in that region are larger. We cannot exclude that a small but nonnegligible time variability near Io's M-shell (Fig. 1) and instrumental effects contribute to this feature. Similarly, shallow negative gradients in oxygen or sulfur PSD profiles at $M \sim 4.7$ and for >180 MeV/(G nucleon) sulfur are insignificant given the systematic and statistical uncertainties involved (see fig. S6 and Materials and Methods, subsection "Uncertainties in HIC spectra"). For this reason, in the follow-up sections, we focus on the potential local oxygen source near Amalthea.

M-shell dependence of energetic heavy ion pitch angle distributions

The inspection of PSD gradients alone is not always sufficient to evaluate the presence of particle sources or sinks. For instance, in the presence of a local particle source, a PSD M-shell gradient could still be positive depending on competing local and nonlocal sink and radial transport processes. Key complementary information is provided through the ions' equatorial pitch angle distributions (PADs). Figure 4 shows M-shell versus equatorial pitch angle (α_{eq}) spectrograms for the four energy channels of HIC shown in Fig. 1. In this plot, the count rate of each HIC channel at any M-shell bin has been normalized to its maximum count rate such that the color coding reveals the shape of the PAD at that M-shell. While these four channels do not separate ion species, we can assume that their shape is most representative for oxygen that dominates for most energy and M-shell ranges considered (Fig. 2), especially for the region of interest near Amalthea, where the potential local ion source resides.

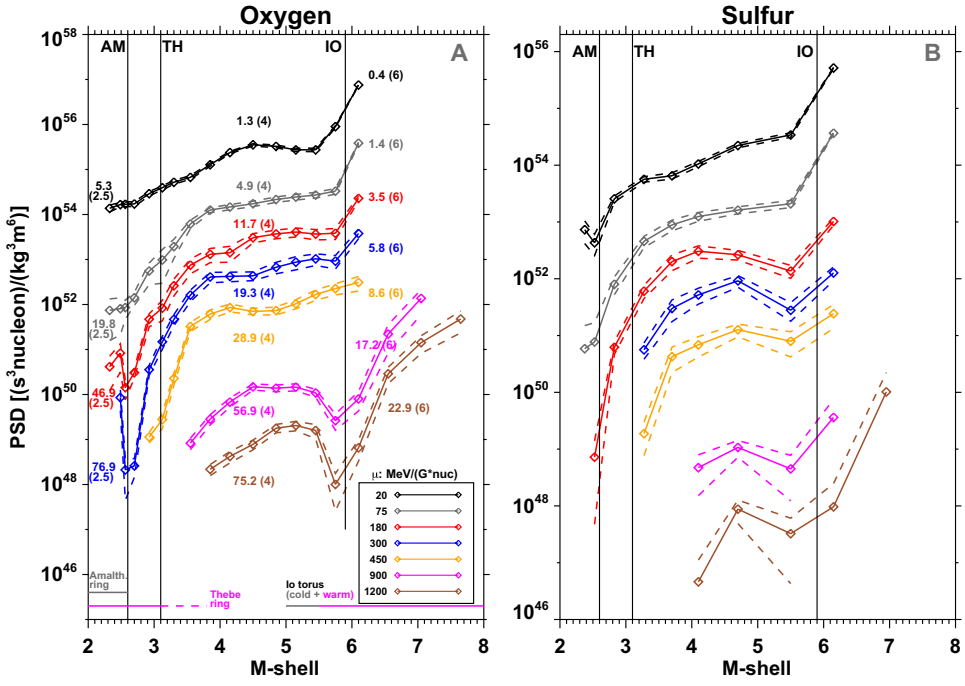

Fig. 3. Energetic oxygen and sulfur phase space densities as a function of M-shell and first adiabatic invariant. (**A** and **B**) PSD M-shell profiles are shown for six selected μ values and $K = 0$ (equatorially mirroring particles) based on orbit A34 data. Numbers along each curve in the oxygen panel show the ion energy in MeV/nucleon for each curve's μ value for an M-shell indicated in the parenthesis. The color coding of the curves and the corresponding energies (in MeV/nucleon) are similar for sulfur. Moons, rings, and the Io torus are marked as in Fig. 1. The lack of phase space density (PSD) estimates for $M > 6.2$ and $\mu < 450$ MeV/(G nucleon) for oxygen and $M > 6.2$ for sulfur is due to the lack of EPD measurements and/or a low number of sulfur events recorded by HIC (fig. S6). Dashed lines indicate the envelope for the uncertainties. When a lower dashed line is absent, it is because the uncertainty is equal or larger than the corresponding PSD. Details on how the PSDs have been obtained are given in Materials and Methods (subsection "Processing of HIC measurements").

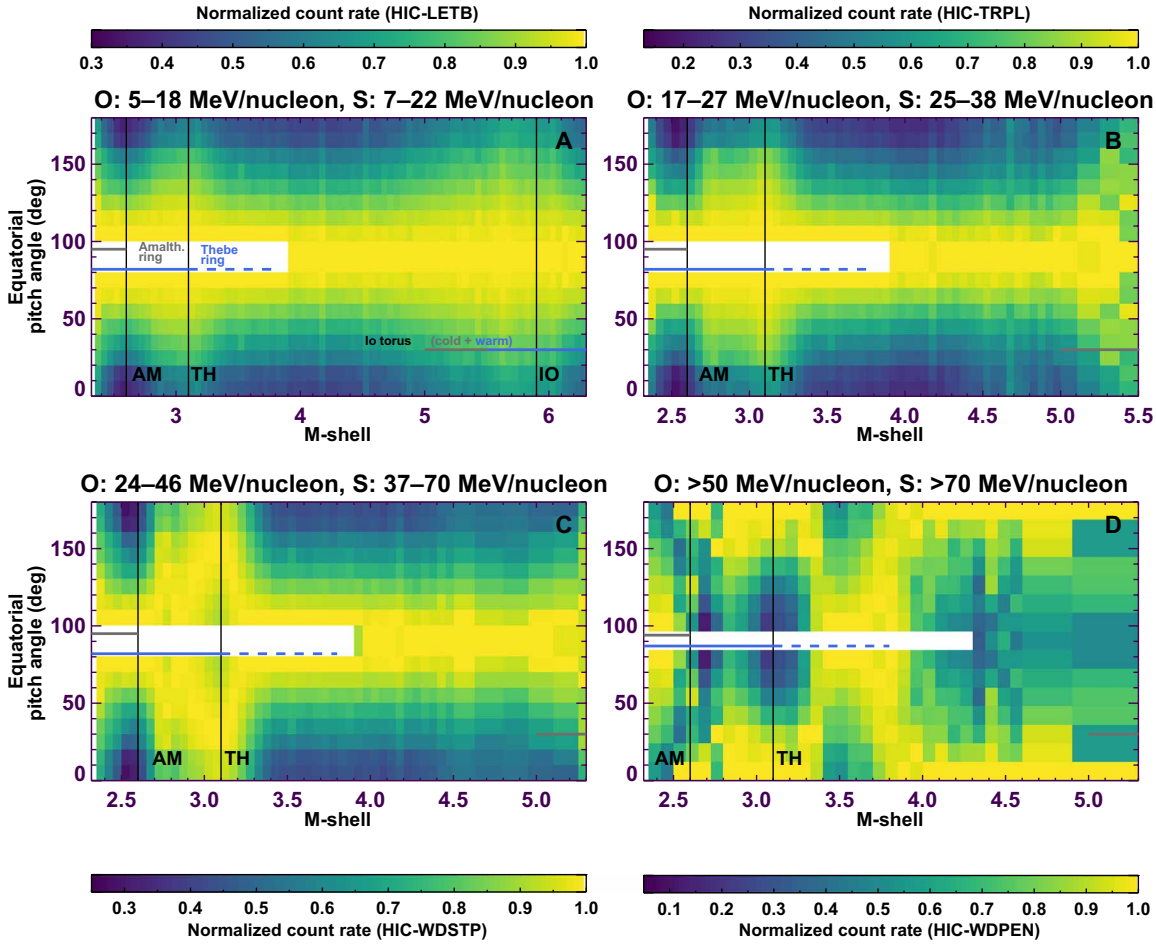

Fig. 4. Energetic ion equatorial PADs. (**A** to **D**) M-shell versus equatorial pitch angle (α_{eq}) for four channels of the HIC instrument based on A34 orbit observations. The highest value at each panel and M-shell bin shows the pitch angle where the signal maximizes. For an improved visual appearance of the data, PADs were constructed assuming pitch angle symmetry, i.e., the signal at α_{eq} is the same as at 180°− α_{eq}. Note that the outward extension of each panel is different, as beyond the selected M-shells, the signal for constructing PADs was too low. Moons, rings, and the Io torus are marked as in Fig. 1. White shaded areas denote equatorial pitch angle ranges that were not sampled. The white band in (D) appears narrower due to the larger binning that is used. Details on how the PADs have been obtained are given in Materials and Methods (subsection "M-shell and pitch angle estimates").

Excluding the >50 MeV/nucleon oxygen channel, measurements at all other energy ranges (Fig. 4, A to C) show trapped distributions typically peaking toward $\alpha_{eq} = 90°$ (pancake PADs). PADs near the Io torus ($M > 5$) and the moon M-shells change their shape as a function of energy. This is possibly related to losses on equatorially confined material (e.g., moons and rings) that tend to reduce the signal of equatorial mirroring ions (*29*, *30*). At low energies (5 to 27 MeV/nucleon), this removal only makes the trapped PADs more isotropic, but with increasing energy, the depletion becomes increasingly deeper until the distribution converts to field-aligned at the highest energies (>50 MeV/nucleon). Inward of Amalthea, HIC resolves an additional PAD broadening at all energies that we only track down to $M \sim 2.2$. We note that because of the offset of Jupiter's dipole from the planet's rotational axis by about 10°, depletions by equatorially confined material should have a shift from $\alpha_{eq} = 90°$ to about 10° to 15° (*29*, *30*), but this shift is too small to be resolved given HIC's angular resolution and uncertainties in pitch angle estimations. We therefore refer to equatorial ion depletions by material as "losses toward $\alpha_{eq} = 90°$."

Contrary to the observations at Thebe and Io, the <50 MeV/nucleon PADs at $2.55 < M < 2.64$, within Amalthea's observed sweeping corridor, show neither a depletion toward $\alpha_{eq} = 90°$ nor a PAD isotropization. Instead, these PADs peak toward $\alpha_{eq} = 90°$, which is unusual for a region where material losses are expected. A minimum toward $\alpha_{eq} = 90°$ at Amalthea is only seen for the >50 MeV/nucleon measurements (Fig. 4D). Despite their negligible signal at Amalthea, however, equatorially mirroring >50 MeV/nucleon ions still evolve into a pancake PAD for $M < 2.6$, as mentioned above. In the context of the lower energy observations, the properties of >50 MeV/nucleon PADs at larger M-shells, which show a field-aligned shape at $M > 4$ that evolves into a pancake distribution within a $\delta M \sim 0.4$ inward of that, are also unusual.

DISCUSSION

In situ energetic particle observations by the Galileo spacecraft presented here reveal that oxygen and sulfur persist as the dominant $Z \geq 4$ species in the largely uncharted region of Jupiter's inner heavy

ion radiation belt at $M < 4.5$ and at >10 MeV/nucleon. Positive PSD gradients observed across wide M-shell and energy ranges (Fig. 3) indicate that adiabatic inward transport continues to be an important heavy ion acceleration process for both species, similarly to what has been resolved for larger M-shells and/or lower energies compared to what we analyze here (*6*, *14*, *16*, *18*). Adiabatic heating is limited by losses at Io, Thebe, and Amalthea as indicated by a variety of ion flux dropout signatures and their corresponding steep positive PSD M-shell gradients at or near the moon M-shells (Figs. 1 and 3 and fig. S6). The fact that these dropout signatures are spatially discrete and become more prominent with increasing energy and toward $\alpha_{eq} = 90°$ indicates that losses at Amalthea and Thebe are primarily driven by ion absorption on their surfaces rather than on the broadly distributed material of the gossamer rings (*31*, *32*). Losses at Io may also have contributions from pitch angle scattering by electromagnetic ion cyclotron (EMIC) waves generated by SO_2^+ and SO^+ ions in its plasma torus (*33*–*35*).

Adiabatic heating and losses largely determine the evolution of oxygen and sulfur distributions toward Thebe and Amalthea. Inward of those moons' M-shells, however, the oxygen abundance relative to sulfur increases considerably, at least up to 100 MeV/nucleon. This change in composition is accompanied by a planetward increase of oxygen PSDs, pointing to a local source of $\gtrsim$50 MeV/nucleon oxygen (Fig. 3). Pancake, instead of isotropic or field-aligned, PADs within the observed Amalthea's sweeping corridor also indicate that there is a process acting to replenish the anticipated oxygen losses. All these signatures complement each other in suggesting that there is a source accelerating or producing very energetic oxygen in the inner radiation belts. The source is best resolved for energies $\gtrsim$50 MeV/nucleon, whereas at much lower energies this source, if present, is overwhelmed by competing processes such as adiabatic transport and losses. Most evidence points to this source residing inward of Amalthea's M-shell, but several indications (e.g., O/S at 7 to 18 MeV/nucleon; Fig. 2C) hint that it could extend as far out as Thebe.

The topology of the source is key for identifying its underlying physical process. For instance, Galileo plasma wave measurements from the A34 orbit show that wave intensities between 5.6 and ~500 Hz increase considerably inside the orbits of Thebe and Amalthea (*36*). This coincidence is noteworthy given that plasma waves with frequencies lower than the oxygen cyclotron frequency (~30 to 300 Hz at Amalthea depending on the oxygen charge state) could, in principle, accelerate oxygen ions through energy diffusion, especially if they are left-hand polarized (EMIC). Wave growth could be the result of charged particle anisotropies associated with their pitch angle–dependent losses at the moon sweeping corridors (*7*, *37*, *38*). It is unclear why a broadband enhancement of wave intensity observed by Galileo (*36*) would preferentially accelerate oxygen over sulfur, because the sulfur cyclotron frequency (~15 to 300 Hz) lies in the same range as that of oxygen. An answer to this question is difficult to obtain given the limitations of Galileo's wave measurements in terms of frequency resolution below 300 Hz and a lack of information on the oxygen and sulfur charge states. We can also not exclude that acceleration is controlled by waves below 5.6 Hz, the properties of which are currently unconstrained. For instance, Alfvèn waves in Earth's inner magnetosphere are considered to be the source of perpendicular ion acceleration, albeit effective only up to ~50 keV (*39*). The anticipated measurements of the plasma, magnetic field, and low-frequency wave environments of the inner radiation belts by Juno would thus offer crucial information for establishing the nature of local heavy ion sources near Amalthea's M-shell.

Another topological coincidence is that of the inferred oxygen source location with Thebe's and Amalthea's rings. Spallation of ring dust may thus be a relevant source process. In the case of energetic ions observed along Jupiter's main ring, it has been proposed that the spallation agents could be trapped gigaelectronvolt protons (*23*). Our simulations (see Fig. 5A and Materials and Methods, subsection "Simulations of ring grain spallation") indicate that while oxygen can be released by proton collisions with 1 to 5 μm of icy dust at Amalthea (*31*), its energies are lower than 1 MeV/nucleon, well below the ~50 MeV/nucleon range indicated by HIC. When the primary spallation agent is 10 to 100 MeV/nucleon sulfur, supplied to the rings through adiabatic transport, oxygen secondaries can have energies as high as 100 MeV/nucleon (Fig. 5B). These secondaries take the form of a broad spectrum of stable ($^{16-18}$O) and unstable isotopes. The most abundant unstable isotope is ^{15}O, which decays into nitrogen within minutes. Unfortunately, HIC does not have the mass resolution to separate ions at neighboring Z-values in its highest energy measurements.

The spallation simulations indicate that ions heavier than oxygen are also released. HIC measures $Z > 8$ ions at >50 MeV/nucleon (events in red dashed line box in fig. S3), but their mass distribution cannot be determined. Some of these predicted secondaries may have a mass similar to sulfur ($Z \sim 16$). However, because a primary magnetospheric sulfur particle can only transfer a lower total energy to its spallogenic products, there is no effective gain for $Z \sim 16$ ions, possibly explaining why the local source seen with HIC is most prominent for ions lighter than sulfur (e.g., oxygen or $Z \sim 8$). Generally, spallation makes the case for the value of energetic particle instruments with high mass resolution, beyond the distinction of protons, helium, oxygen, and sulfur that is a minimum standard at Jupiter.

A caveat of the spallation scenario is that it appears to be much more efficient for generating low-Z ions than oxygen (e.g., helium), as only about 10^{-4}% of the ion-dust collisions would release a $Z \sim 8$ ion with the right energy in the magnetosphere. The low probability of sulfur ions colliding with dust in Jupiter's tenuous rings (*31*, *35*) would reduce this efficiency even further. Oxygen itself may also act as a spallation agent for lower mass secondaries and is subject to ring losses. What could balance the low secondary ion production efficiency is that the fluxes of magnetospheric sulfur, e.g., at 50 MeV/nucleon (fig. S6), are up to seven orders of magnitude higher than the GCR and ACR fluxes that power Earth's and Saturn's proton and heavy ion radiation belts through material interactions (e.g., CRAND) (*8*, *22*, *40*). Oxygen ring losses could be balanced through ring spallation by multiple species heavier than oxygen besides sulfur, such as sodium (*15*). Long lifetimes against radial transport [more than 20 years at Amalthea based on estimated radial diffusion rates (*35*)] could potentially allow spallogenic products to accumulate to the observed flux levels.

In conclusion, Galileo observations by its HIC and EPD instruments provide us with one of the most detailed descriptions of Jupiter's inner heavy ion radiation belt to date in terms of radial profile, ion composition, energy spectra, and angular distributions. We find that the distribution of its dominant heavy ion species, oxygen and sulfur, is in part shaped by adiabatic heating and material-driven losses, processes that are known to act in all outer planet

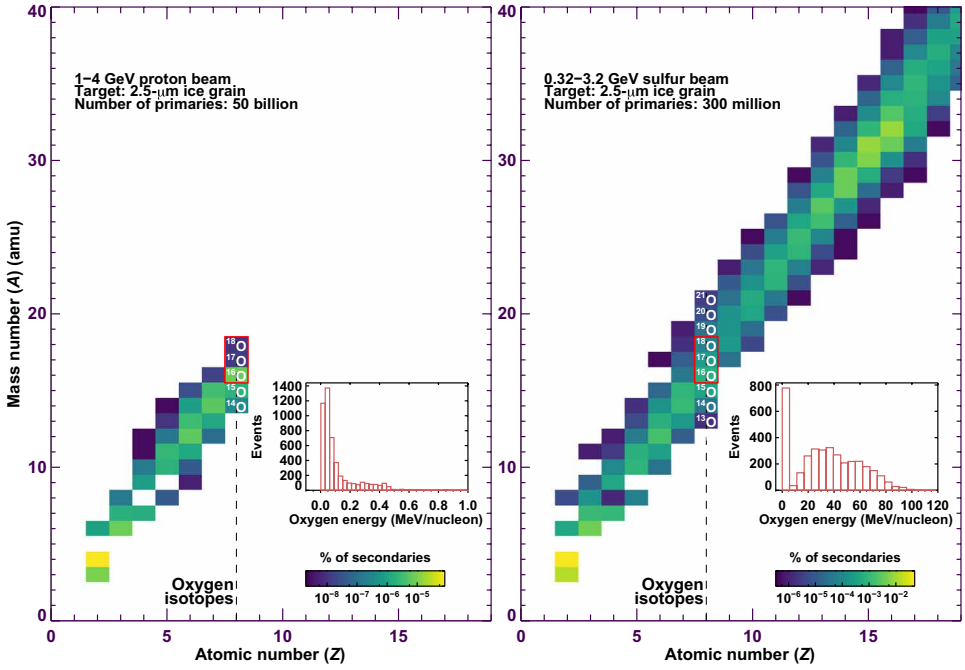

Fig. 5. Simulation of secondary ions and isotopes released from the irradiation of water ice grains with gigaelectronvolt protons and sulfur. Both plot panels show the simulated isotopic and energy distributions of $Z \geq 2$ secondary ions following the irradiation of water ice grains with a radius of 2.5 μm by protons (left) and sulfur (beams). $Z = 1$ isotopes and neutrons are also produced but were not tracked. Oxygen isotopes are highlighted, with those in a red box corresponding to the stable ones. The color scale indicates the probability (in percentage) that a certain isotope is released from a grain per collision. The insets show the energy distribution of all secondary oxygen isotopes.

radiation belts. In addition, excess oxygen PSDs and an increased abundance of oxygen show that a source of ≳50 MeV/nucleon oxygen located planetward of Thebe's or Amalthea's M-shell is also acting. Candidate physical processes driving this local source are different from the known ion sources at Earth and Saturn. If oxygen derives from the spallation of Jovian ring grains, it could classify Jupiter's heavy ion belt as a self-sustained radiation belt system where the primary spallation agent is generated internally to the magnetosphere in the form of adiabatically heated gigaelectronvolt sulfur. Such a configuration is fundamentally different to an ion radiation belt system that is being supplied externally through pre-accelerated GCRs or ACRs (*22*, *41*). A similar process has been invoked to explain the presence of trapped heavy ions in astrophysical radiation belts that enclose orbiting material within their volume (*42*). If the source is instead driven by turbulent oxygen heating, this would be the first time that an observational baseline is established for understanding stochastic ion acceleration to gigaelectronvolt energies in a stable magnetospheric environment, a process that is otherwise believed to occur in stellar magnetic field environments [e.g., solar flares (*43*, *44*)]. Irrespective of the exact process responsible for the observed ion acceleration, the colocation of the oxygen source with the orbits of Thebe and Amalthea and/or their rings and hints of a similar >10 MeV/nucleon source within the boundaries of the dense Io torus suggest the existence of additional pathways through which magnetospheres containing significant amounts of neutral material within their volume can generate particle radiation with cosmic ray energies.

MATERIALS AND METHODS

Instrumentation and datasets

Heavy ion counter

The primary dataset used in the present work comes from the HIC instrument of the Galileo mission (*24*). HIC data, excluding the time-dependent (pitch angle) pointing of HIC, the calculation of which is described in the "M-shell and pitch angle estimates" subsection of Materials and Methods, are provided through the Planetary Data System (PDS) (https://pds-ppi.igpp.ucla.edu/mission/Galileo/GO/HIC). HIC was designed to measure the composition of $Z \geq 6$ ions (carbon or heavier), but under certain configurations, it could also detect $Z \geq 4$ ions (lithium or heavier). HIC comprised two particle telescopes named as LET-B and LET-E. LET-B measured the composition and the spectra of energetic heavy ions between about 5 and 25 MeV/nucleon. It consisted of a stack of four SSDs named as LB1 to LB4 and arranged on a cylindrical assembly with conical aperture of a 25° half-angle upstream of the LB1 SSD. The LET-E telescope has the same configuration as LET-B but contains five SSDs (named LE1 to LE5), and it was sensitive to >15 MeV/nucleon ions. The LET-E detectors were assembled in a stack with an effective aperture of 25° to 75° half-angle, depending on the combinations of SSDs used and the energies of the particles considered (fig. S1). Both telescopes used coincident energy losses of ions on multiple SSDs to resolve different ion species and their energies through the ΔE × E technique (*45*). The channels are named (from lowest to highest energies) LETB, DUBL, TRPL, WDSTP, and WDPEN. Here, only the first and the last three channels are used

(e.g., Fig. 1 and table S1), with LETB belonging to the LET-B telescope and the rest to LET-E.

The coincidence channels of HIC return two types of measurements: the rate data, where particle events satisfying the coincident logic of a channel were counted over intervals that depend on the time resolution that HIC operates (Fig. 1), and the pulse height analyzed (PHA) data, where for a small subset of the aforementioned events the ionizing energy losses on three selected HIC SSDs (or sum of SSDs) were downlinked (table S1). PHA data are necessary to distinguish the relative contributions of the different ion species and energies, but their low counts mean that multiple directions and times (locations) have to be averaged together to create statistically significant spectra. The rate channels provide a more statistically significant signal to derive high spatial and pitch angle resolution observations, but mix multiple species and energies. PHA and rate data are linked through a livetime (T_{LV}), which normalizes the small data sample of PHA events to the larger sampling of the rate channels (*46*, *47*). The DUBL channel of telescope LET-E returned PHA but not rate data for most of the A34 orbit, which is why it was not used.

Composition measurement system of the energetic particle detector

The EPD of Galileo (*25*) consisted of multiple sensor modules, distributed on two instrument assemblies, the low-energy magnetospheric measurement system (LEMMS) and the CMS. Only CMS has ion composition capabilities, which is why it was used here. EPD/CMS alone comprised two ends, separated by 180° in pointing. The one end of CMS had a single-particle telescope using time-of-flight (TOF) and energy loss measurements on an SSD (TOF × E technique) to obtain the spectrum of protons and heavy ions. Its measurements were saturated for most part of the A34 orbit, and they were not used. The opposite end contained two telescopes, each with a double SSD stack, using the same measurement principle as HIC (ΔE × E) and were sensitive to $Z \geq 2$ ions of ≥ 0.27 MeV/nucleon. From these two telescopes, one was switched off in 1997.

Because of data rate limitations, the telescopes operated only during selected high–time resolution intervals of the mission, and their data have not been used as extensively as the TOF × E measurements of CMS, excluding one case (*48*). Because the A34 orbit was one of these high–time resolution intervals, ΔE × E measurements by CMS are available, albeit for shorter intervals compared to HIC (only inward of $M \sim 6.2$ for A34). Similar to HIC, these CMS telescopes returned both PHA and rate data, but in addition, the rate data were further binned onboard EPD in multiple channels to provide a rough separation at least between several major species like sulfur, oxygen, helium, and sodium/magnesium and energies. We directly used the measurements of these channels here, which were recently reprocessed (*49*). A minimal additional processing, specific to orbit A34, is described below.

Oxygen channels used are CM1 and CM3 to CM5 (0.29 to 5.6 MeV/nucleon), while for sulfur, we used CH1, CH3, and CH4 (0.27 to 0.93 MeV/nucleon). A visual definition of these channels is shown in fig. S7. A fourth sulfur channel (CH5: 4.4 MeV/nucleon) was not used because its corresponding fluxes were considerably lower from those of HIC at neighboring energy ranges and more than a factor of 10 below past estimates for similar energies (*16*). We attribute this mismatch to possible issues with the CH5 calibration parameters rather than to HIC. We consider HIC as more reliable because it has ~40 times larger geometry factor than EPD at similar energies. The reason we use EPD/CMS despite its limitations is primarily for extending the M-shell and magnetic moment ranges over which PSD profiles could be constructed and for validating the HIC pitch angle and flux estimates at neighboring energy ranges of the two instruments.

Processing of HIC measurements

HIC ion flux and PSD estimates

To convert HIC count rates to fluxes, we followed the procedure described in earlier investigations where HIC data were used to derive heavy ion spectra beyond Io's orbit (*47*). Starting from the PHA data, we estimate the events that correspond to our species of interest (oxygen or sulfur) and assign an energy to them based on our calibration that we describe below. We then group the PHA events in predefined energy and M-shell bins, where for each combination the flux is estimated as

$$j(E_i, L) = \sum_{i=1}^{N} \frac{1}{NG(E_i)\,\Delta E\,T_{LV(i)}} \quad (1)$$

Here, we bin particles in M-shell and in ambient energy within the magnetosphere. E_{min} and E_{max} are the bin boundaries. E is geometric mean of a predefined energy bin, with $E = \sqrt{E_{min}\,E_{max}}$ and $\Delta E = E_{max} - E_{min}$. The conversion between the ambient ion energy in the magnetosphere, E, and the energies deposited in various SSDs is discussed below. We sum over every N time tag within the respective bin. Last, $G(E_i)$ and $T_{LV(i)}$ are the energy-dependent geometry factor (discussed in the "HIC calibration updates" subsection of Materials and Methods and shown in fig. S2) and the livetime (provided in the archived HIC dataset) of the "ith" valid PHA event, respectively. The way that M-shell and energy bins were selected was based on a balance of counting statistics and also the uncertainties in energy determination. For example, because for the highest energy measurements by the WDPEN channel of the LET-E telescope (≫50 MeV/nucleon oxygen) the uncertainty in energy determination was typically >50%, we decided to use a single energy bin for the regime reaching 100 MeV/nucleon. Our spectra are in good agreement with those obtained by the Voyager spacecraft and/or Galileo/HIC for the J0 orbit (*16*), as well as with spectra estimated slightly outward of Io (*46*, *47*).

Phase space densities are estimated directly from the spectra at the geometric mean energies of the corresponding magnetic moments, μ. For intermediate E and μ values, we use linear interpolation in the (log(E),log(j)) space. Because the orbit of Galileo was close to the magnetic equator and almost all equatorial pitch angles were sampled and the pitch angle contrast of the signal is small, we estimated PSDs at constant μ by assuming that the omnidirectional spectra are representative for equatorially mirroring ions ($\alpha_{eq} = 90°$), similar to earlier studies (*14*, *16*).

HIC calibration updates

The HIC PDS dataset provides energy and species information for each PHA event, but we did not use it here for several reasons. The first is because the method used to invert the PHA event data (*14*, *16*, *45*, *50*) requires that particles are stopped in the SSDs, a case that does not apply for the WDPEN channel (fig. S1). The second reason is that the PDS inversions relied on the calibration of HIC at the beginning of the mission, which is not fully applicable for the last Galileo orbits: Because of the exposure of HIC's detectors on the radiation environment of Jupiter, the upstream SSDs of LET-B

(LB1 and LB2) and LE1 of LET-E developed dead layers by the time of the A34 orbit, making their effective thickness over which ionizing energy losses are recorded smaller. The development of dead layers has also been reported for the TOF × E system of EPD/CMS (*51*) and also affected its ΔE × E telescope (fig. S7). Because dead layers are not considered in the PDS calibration, inversions of PHA data that clearly belong to oxygen and sulfur events assign masses of ~14 and ~27 atomic mass units (amu) instead of 16 and 32 amu, respectively (fig. S4). This also induces systematic errors in the ambient energy determination of each event.

To account for the dead layer, we used range-energy tables to calculate energy tracks deposited in the detectors for sulfur and oxygen. The tables were generated through the SRIM software (*52*). Required information on HIC's geometric characteristics and detector sizes was obtained from www.srl.caltech.edu/galileo/SRD/srd2.html and the instrument description paper (*24*). By varying detector (and dead layer) thicknesses and by comparing the energy loss curves with HIC's PHA measurements, we estimated that SSDs LB1, LB2, and LE1 have dead layers comprising 25, 2.5, and 10% of their original thickness, whereas all other detectors were unaffected. On the basis of the resulting simulated energy loss curves for different incidence angles (Fig. 2, A and B), we specified the regimes for each ion species and defined which events could be classified as oxygen or sulfur (fig. S3).

After the species were defined, we used the simulated energy loss curves per SSD (or sum of SSDs) to convert the measured energy losses into the ambient ion energy per nucleon in the magnetosphere. Where possible, we used multiple SSD combinations and/or multiple ion incidence angles to minimize the errors in species and energy determination. For the highest energy events of HIC that are recorded with channel WDPEN, which measures ions that can fully penetrate all detectors of the LET-E telescope, it was necessary to rely on assumptions about which species dominates, as discussed in the context of Fig. 2.

For the estimation of the energy-dependent geometry factor [$G(E)$], we performed simulations using GEANT4 Monte Carlo simulations, as in (*10*). The simulations were performed only for the LET-E telescope, because for LET-B a uniform geometry factor of 0.429 cm^2 sr across its energy response (passband) was found to be sufficient (*46*, *47*). PDS provides energy-independent values of G, which are a good approximation except at the edges of the LET-E channel responses. Furthermore, it does not take into account instrument penetrating heavy ions captured mostly by channel WDPEN. The aluminum shielding of the HIC model was based on an inspection of the telescope's drawings (*24*, *46*, *47*). For a higher efficiency in the calculations and for better particle statistics, no spacecraft shielding was considered. The spacecraft shielding primarily reduces the ions accessing the SSDs from the backside of HIC, but even when this is neglected, backward penetrating ions have little contribution to the geometry factor of its channels. GEANT4 simulation results also validated the energy loss curves simulated with the simple range-energy tables.

M-shell and pitch angle estimates

Magnetic field estimates were used for the magnetic mapping of HIC's and EPD's measurements, the estimation of μ, and the conversion of local to equatorial pitch angle. For that purpose, we used a Jovian magnetic field model (JRM09) coupled with a model for a current sheet (CAN) (*53*). Hence, the term "M-shell" was used (as introduced for Juno mission investigations), instead of "L-shell." Galileo magnetometer data were not used because they saturate approximately inward of $M \sim 3$. For $M > 3$, we only used the magnetometer data to verify that differences between a data and a model-derived pitch angle were insignificant.

Both HIC telescopes had a fixed mounting on Galileo's rotating platform (rotor) and thus were sampling different directions as the rotor was spinning with a period of 20 s. The pointing of HIC was reconstructed on the basis of rotor data available in https://pds-ppi.igpp.ucla.edu/search/view/?id=pds://PPI/GO-J-POS-6-REDR-ROTOR-ATTITUDE-V1.0 and information for the fixed HIC pointing on rotor coordinates. Information on the exact pointing was obtained directly from HIC team members, as the vector provided through NASA's Navigation and Ancillary Information Facility (NAIF) is invalid (see table S1). For obtaining the pitch angle pointing of HIC, we used only the highest time resolution intervals, where the spin of Galileo's rotor is resolved. Another important correction was applied by subtracting the buffering time (transmission time between data accumulation from the sensor and onboard processing storage), which is not taken into account in the measurement time tags available in the archived PDS dataset (see table S1). A buffering time correction of 2.5 s was chosen on the basis of the HIC documentation. Without this correction, pitch angle values would have a systematic offset up to 22.5°. Validated pitch angle values of EPD/CMS are provided directly through the reprocessed EPD dataset, with a caveat that data from certain pointing directions have been removed because of spacecraft obscuration and/or contamination by a radioactive calibration source on EPD (*49*). Construction of EPD/CMS PADs (figs. S8 and S9) serves the additional purpose of validating the HIC pitch angle estimates, by showing how PADs of these instruments are similar at their overlapping energy ranges.

Uncertainties in HIC spectra and phase space densities

The uncertainty ranges in fig. S6 are primarily controlled by Poisson statistics, i.e., the value of N. Most of the M-shell and energy bins contained at least 15 valid PHA samples, with few exceptions for the highest energy measurements of sulfur and oxygen by the WDPEN channel. In total, we classified 4580 valid oxygen and 953 valid sulfur PHA events, resulting on an average of 60 and 20 events per M-shell and energy bin, respectively, for the spectra of fig. S6. Smaller and relatively negligible contributions arise from uncertainties in the livetime normalization (T_{LV}).

Systematic uncertainties are not only more significant but also difficult to quantify. The number of events identified as oxygen and sulfur may have been overestimated. Because of ion scattering on the HIC SSDs, the energies of the PHA events spread out of the ranges defined by the simulated energy loss curves (Fig. 2). For this reason, we manually enlarged these ranges (fig. S3). To account for a possible overestimation of the number of valid PHA events we assign to a given species, we made the extreme assumption that our statistical sample per energy and M-shell bin can be up to 30% lower, i.e., 30% of the events have been mistagged. Even in that case, the error bars remain small compared to the variability of the radial profiles, with an exception of the region near Io and the energy regime near 100 MeV/nucleon. Another systematic feature with uncertain interpretation is that of large count rate spikes, most clearly seen in channels TRPL and WDSTP (Fig. 1, B and C). The fact that they are seen in later orbits rather than the first one (J0) and only in LET-E channels suggests that they may be a feature

associated with either the aging of LET-E or a different operation mode of that sensor. The spikes are very prominent for $M > 5$ and may lead to some flux overestimations in that region, which is one more reason we refrain from conclusively interpreting planetward PSD rises near Io in the present study.

Another source of error may be the estimation of the ions' energies from our calibration curves. By using PHA measurements to convert the energy loss of an ion on at least two SSDs, we find that the energy uncertainty for channels LETB, TRPL, and WDSTP is typically below 30%, but for WDPEN, it can be as large as 70%. To minimize the impact of these uncertainties, we defined only four energy bins for estimating oxygen and sulfur spectra from HIC. Using smaller energy bins, with a width as low as the energy uncertainty, did not offer any advantages and, at the same time, decreased the available events per M-shell and energy bin. This uncertainty in energy determination also affects how well we can constrain the energy regime of the local oxygen source. The planetward oxygen PSD rise is clear above 50 MeV/nucleon. Below that range, HIC oxygen measurements come from the WDSTP channel, for which the oxygen energy determination uncertainty is small. Thus, the 30 MeV/nucleon lower limit for the source is determined mostly by monitoring at which μ the PSD rise becomes insignificant.

Inspection of the cluster of WDPEN (oxygen) events below LE3 = 100 MeV (points enclosed in the green dashed line and the blue solid line boxes in fig. S3D) shows that the events deviate from the expected energy loss tracks (black curves) at low LE3 energy losses (LE3 below about 50 to 60 MeV). Events spread over a quasi-constant LE4 + LE5 energy loss range. We have compared the shown cluster of WDPEN events from the radiation belts with measurements taken at large distances from Jupiter, including time periods close to the A34 orbit, when WDPEN was dominated by penetrating GCRs instead of (potential) radiation belt ions (*54*). These events distribute parallel to the energy loss curves (fig. S5), as expected, suggesting that the clustering of event data at quasi-constant LE4 + LE5 energy seen at A34 is not an artifact of the channel that always existed or resulted from degradation of the LET-E telescope.

The main difference between the GCR and the radiation belt response is the much higher ion flux in the latter. We also note that WDPEN uses quadruple coincidence and no anticoincidence. In a high flux environment, it is not unlikely that one of the four detector hits is accidental. This means that one of the four detectors is triggered by a separate particle than the one that triggers the other three SSDs. However, we cannot be certain on which detector the accidental event occurs. Simplified simulations of accidental coincidences using random event selections from our GEANT4 simulation results suggest that the most affected detector is likely LE5, meaning that the stronger contrast in LE3 energy losses can be used to map the ambient oxygen energy associated with each WDPEN PHA event. With that in mind, we estimate that oxygen ions may have energies as high as 300 MeV/nucleon. Despite that, we choose to be conservative and assume that all events that significantly deviate from the tracks (LE3 < 55 MeV) are accidentals and ignore them. The reason is that because in a high flux region a single accidental hit on LE5 may be enough to trigger a WDPEN signal, the effective geometry factor of the channel is much higher than its nominal one, especially for the most efficiently penetrating ions ($\gtrsim$140 MeV/nucleon oxygen or LE3 $\lesssim$ 50 to 60 MeV). We thus keep only the LE3 $\gtrsim$ 55 MeV events for spectral analysis (<140 MeV/nucleon).

The plotted uncertainties in PSD (Fig. 3) propagate directly from the uncertainties in fluxes. Our assumption that PSDs are representative for equatorially mirroring ions is not inducing any appreciable errors that could affect sharp PSD gradients, given the low pitch angle contrast of the HIC signal. If PADs are considered, they would actually make our case for a local oxygen source inward of Amalthea stronger because >50 MeV/nucleon PADs at Amalthea's sweeping corridor peak in the field aligned direction, whereas inward of that they peak at $\alpha_{eq} = 90°$. Generating pitch angle–dependent PSDs requires to separate the mixed energies and ion species in the high spatial resolution PAD profiles (Fig. 4) and the mixed pitch angle information in the low spatial and angular resolution spectral profiles (fig. S6), a task that is not free of assumptions.

Processing of EPD measurements

Because EPD measurements were used here mostly for providing additional context to the highest energy ion observations of HIC, the processing steps applied were simpler. We obtained the differential number fluxes of oxygen and sulfur by binning the count rates of the CM and CH channels in the same M-shell bins as HIC and then applying

$$j_i(E,L) = c_i \frac{R_i}{g\,\Delta E_i} \tag{2}$$

For the *i*th channel of EPD at an M-shell, M, R_i is the corresponding count rate and ΔE_i is the channel's passband. The geometric factor, g, was taken to be 0.008 cm^2 sr for all channels (*49*).

The constant c_i is a correction factor used to account for the spread of sulfur counts into neighboring channels due to the dead-layer buildup on EPD's SSDs for orbit A34 (fig. S7). We estimated this factor by generating PHA count histograms and by calculating the fraction of the sulfur peak that spreads outside a CH-channel box boundary. For channels CH3 and CH4, c_i is 1.15 and 1.4, respectively. For oxygen channel CM3, this factor is 0.85, because sulfur counts drift into the channel's regime, increasing its count rate. For other channels, $c_i = 1$, because PHA count statistics were not sufficient to make an evaluation (CM1, CH1, CH5), or because they were negligibly affected by dead-layer effects (CM4, CM5). The correction factor c_i only shifts the absolute number of counts in a channel at a given time, and it is not dependent on particle pitch angle. Note also that the values of c_i provided here are applicable only for orbit A34, and they should converge toward unity for earlier phases of the mission.

Scattered counts in PHA boxes that clearly do not belong to oxygen or sulfur (most visible at CM3) are mostly due to instrument penetrating radiation, for which a correction is already provided in the archived EPD dataset (*49*). The uncertainty range in the fluxes of the EPD channels is basically controlled by the Poisson error on their counting rate, R_i.

Simulations of ring grain spallation

Simplified simulations of ring grain spallation were set up and performed with GEANT4 (*55*). The goal was to principally understand what type of heavy ion secondaries and with what energy are released for different spallation agents. In Fig. 5, spherical grains with a radius of 2.5 μm and an ice composition were defined as the targets to be irradiated by a unidirectional, point source (beam) of protons or sulfur. These ion beams had uniform energy distributions, with energies ranging between 1 and 4 GeV for protons and

0.32 and 3.2 GeV (10 to 100 MeV/nucleon) for sulfur. Varying the radius of the grains between 1 and 5 μm does not affect our conclusions. The assumptions for the ring grain size are based on their measured distribution during the A34 and J35 orbits by Galileo's dust detector (*31*). No detailed information exists on the grains' composition, which is why we assumed here that they comprise pure ice, on the basis that the gossamer rings derive from collisional ejecta of Amalthea and Thebe (*56*) and that the dominant constituent of Amalthea is ice (*57*). Other studies, mostly focused on Jupiter's main ring, have used a rocky composition [e.g., (*58*)], whereas certain investigations indicate that Amalthea also likely has non-ice admixtures on its surface (*59*). A varying composition for the spallation target was beyond the scope of our simulations but should be considered in follow-up works.

A single grain target was used in each simulation. The total ion energy was chosen such that there is the possibility to knock out a secondary oxygen with at least 10 MeV/nucleon (or 160 MeV) kinetic energy, if there is significant energy transfer from the primary. The simulation was configured so as to allow the generation of all types of secondaries, including photons, electrons, neutrons, and $Z \geq 1$ isotopes. For the output, we tracked only $Z \geq 2$ isotopes to improve the processing speed, because the number of protons and neutrons generated could be more than 30 times higher than that of any other secondary. The secondaries were registered only when they escaped the icy grain. After the secondaries were registered, they were immediately deleted; thus, the decay process of unstable isotopes was not simulated. In proton beam simulations, we injected 50 billion primaries, whereas 300 million primaries were used for sulfur. The primary particle inducing the spallation reaction typically penetrated through the icy grain, excluding the few times it transferred much of its energy to the secondary ions. The GEANT4 simulations do not offer information on the charge state of secondary ions. For the estimation of the percentage of secondary ions escaping the grain (Fig. 5), we assumed that all secondaries are charged.

SUPPLEMENTARY MATERIALS

Supplementary material for this article is available at https://science.org/doi/10.1126/sciadv.abm4234

REFERENCES AND NOTES

1. B. H. Mauk, N. J. Fox, Electron radiation belts of the solar system. *J. Geophys. Res. Space Phys.* **115**, A12220 (2010).
2. B. H. Mauk, Comparative investigation of the energetic ion spectra comprising the magnetospheric ring currents of the solar system. *J. Geophys. Res.* **119**, 9729–9746 (2014).
3. E. Roussos, P. Kollmann, *The Radiation Belts of Jupiter and Saturn* (American Geophysical Union, 2021), chap. 32, pp. 499–514.
4. S. J. Bolton, M. Janssen, R. Thorne, S. Levin, M. Klein, S. Gulkis, T. Bastian, R. Sault, C. Elachi, M. Hofstadter, A. Bunker, G. Dulk, E. Gudim, G. Hamilton, W. T. K. Johnson, Y. Leblanc, O. Liepack, R. McLeod, J. Roller, L. Roth, R. West, Ultra-relativistic electrons in Jupiter's radiation belts. *Nature* **415**, 987–991 (2002).
5. Q. Nénon, A. Sicard, S. Bourdarie, A new physical model of the electron radiation belts of Jupiter inside Europa's orbit. *J. Geophys. Res. Space Phys.* **122**, 5148–5167 (2017).
6. P. Kollmann, G. Clark, C. Paranicas, B. Mauk, E. Roussos, Q. Nénon, H. B. Garrett, A. Sicard, D. Haggerty, A. Rymer, Jupiter's ion radiation belts inward of Europa's orbit. *J. Geophys. Res.* **126**, e2020JA028925 (2021).
7. R. S. Selesnick, A. C. Cummings, J. R. Cummings, R. A. Mewaldt, E. C. Stone, T. T. von Rosenvinge, Geomagnetically trapped anomalous cosmic rays. *J. Geophys. Res.* **100**, 9503 (1995).
8. R. S. Selesnick, D. N. Baker, S. G. Kanekal, V. C. Hoxie, X. Li, Modeling the proton radiation belt with Van Allen probes relativistic electron-proton telescope data. *J. Geophys. Res.* **123**, 685–697 (2018).
9. T. P. Armstrong, S. Taherion, J. Manweiler, S. Krimigis, C. Paranicas, D. Mitchell, N. Krupp, Energetic ions trapped in Saturn's inner magnetosphere. *Planet. Space Sci.* **57**, 1723–1731 (2009).
10. E. Roussos, P. Kollmann, N. Krupp, A. Kotova, .L Regoli, C. Paranicas, D. G. Mitchell, S. M. Krimigis, D. Hamilton, P. Brandt, J. Carbary, S. Christon, K. Dialynas, I. Dandouras, M. E. Hill, W. H. Ip, G. H. Jones, S. Livi, B. H. Mauk, B. Palmaerts, E. C. Roelof, A. Rymer, N. Sergis, H. T. Smith, A radiation belt of energetic protons located between Saturn and its rings. *Science* **362**, eaat1962 (2018).
11. J. A. van Allen, B. A. Randall, D. N. Baker, C. K. Goertz, D. D. Sentman, M. F. Thomsen, H. R. Flindt, Pioneer 11 observations of energetic particles in the Jovian magnetosphere. *Science* **188**, 459–462 (1975).
12. J. A. Simpson, D. C. Hamilton, G. A. Lentz, R. B. McKibben, M. Perkins, K. R. Pyle, A. J. Tuzzolino, J. J. O'Gallagher, Jupiter revisited: First results from the University of Chicago charged particle experiment on pioneer 11. *Science* **188**, 455–459 (1975).
13. K. R. Pyle, R. B. McKibben, J. A. Simpson, Pioneer 11 observations of trapped particle absorption by the Jovian ring and the satellites 1979, J1, J2, and J3. *J. Geophys. Res.* **88**, 45 (1983).
14. N. Gehrels, E. C. Stone, J. H. Trainor, Energetic oxygen and sulfur in the Jovian magnetosphere. *J. Geophys. Res.* **86**, 8906 (1981).
15. T. L. Garrard, E. C. Stone, N. Murphy, Effects of absorption by Io on composition of energetic heavy ions. *Science* **274**, 393–394 (1996).
16. C. M. S. Cohen, T. L. Garrard, E. C. Stone, J. F. Cooper, N. Murphy, N. Gehrels, Io encounters past and present: A heavy ion comparison. *J. Geophys. Res.* **105**, 7775–7782 (2000).
17. B. H. Mauk, D. G. Mitchell, R. W. McEntire, C. P. Paranicas, E. C. Roelof, D. J. Williams, S. M. Krimigis, A. Lagg, Energetic ion characteristics and neutral gas interactions in Jupiter's magnetosphere. *J. Geophys. Res.* **109**, A09S12 (2004).
18. J. D. Anglin, J. R. Burrows, J. L. Mu, M. D. Wilson, Trapped energetic ions in Jupiter's inner magnetosphere. *J. Geophys. Res.* **102**, 1–36 (1997).
19. D. K. Haggerty, B. H. Mauk, C. P. Paranicas, G. Clark, P. Kollmann, A. M. Rymer, G. R. Gladstone, T. K. Greathouse, S. J. Bolton, S. M. Levin, Jovian injections observed at high latitude. *Geophys. Res. Lett.* **46**, 9397–9404 (2019).
20. H. N. Becker, J. W. Alexander, J. E. P. Connerney, M. J. Brennan, A. Guillaume, V. Adumitroaie, M. M. Florence, P. Kollmann, B. H. Mauk, S. J. Bolton, High latitude zones of GeV heavy ions at the inner edge of Jupiter's relativistic electron belt. *J. Geophys. Res.* **126**, e2020JE006772 (2021).
21. E. Roussos, E. Roussos, N. Krupp, T. P. Armstrong, C. Paranicas, D. G. Mitchell, S. M. Krimigis, G. H. Jones, K. Dialynas, N. Sergis, D. C. Hamilton, Discovery of a transient radiation belt at Saturn. *Geophys. Res. Lett.* **35**, L22106 (2008).
22. R. S. Selesnick, E. C. Stone, Energetic electrons at Uranus: Bimodal diffusion in a satellite limited radiation belt. *J. Geophys. Res.* **96**, 5651 (1991).
23. H. M. Fischer, E. Pehlke, G. Wibberenz, L. J. Lanzerotti, J. D. Mihalov, High-energy charged particles in the innermost Jovian magnetosphere. *Science* **272**, 856–858 (1996).
24. T. L. Garrard, N. Gehrels, E. C. Stone, The Galileo heavy element monitor. *Space Sci. Rev.* **60**, 305 (1992).
25. D. J. Williams, R. W. McEntire, S. Jaskulek, B. Wilken, The Galileo energetic particles detector. *Space Sci. Rev.* **60**, 385–412 (1992).
26. J. F. Cooper, Nuclear cascades in Saturn's rings: Cosmic ray albedo neutron decay and origins of trapped protons in the inner magnetosphere. *J. Geophys. Res.* **88**, 3945–3954 (1983).
27. C. Paranicas, D. G. Mitchell, S. M. Krimigis, D. C. Hamilton, E. Roussos, N. Krupp, G. H. Jones, R. E. Johnson, J. F. Cooper, T. P. Armstrong, Sources and losses of energetic protons in Saturn's magnetosphere. *Icarus* **197**, 519–525 (2008).
28. P. Kollmann, E. Roussos, C. Paranicas, N. Krupp, D. K. Haggerty, Processes forming and sustaining Saturn's proton radiation belts. *Icarus* **222**, 323–341 (2013).
29. P. Kollmann, C. Paranicas, G. Clark, E. Roussos, A. Lagg, N. Krupp, The vertical thickness of Jupiter's Europa gas torus from charged particle measurements. *Geophys. Res. Lett.* **43**, 9425–9433 (2016).
30. Q. Nénon, N. André, Evidence of Europa neutral gas torii from energetic sulfur ion measurements. *Geophys. Res. Lett.* **46**, 3599–3606 (2019).
31. H. Krüger, D. P. Hamilton, R. Moissl, E. Grün, Galileo in-situ dust measurements in Jupiter's gossamer rings. *Icarus* **203**, 198–213 (2009).
32. E. Roussos, N. Krupp, P. Kollmann, C. Paranicas, D. G. Mitchell, S. M. Krimigis, M. Andriopoulou, Evidence for dust-driven, radial plasma transport in Saturn's inner radiation belts. *Icarus* **274**, 272–283 (2016).
33. M. F. Thomsen, Jovian magnetosphere-Satellite interactions: Aspects of energetic charged particle loss. *Rev. Geophys. Space Phys.* **17**, 369 (1979).
34. X. Blanco-Cano, C. T. Russell, R. J. Strangeway, The Io mass-loading disk: Wave dispersion analysis. *J. Geophys. Res.* **106**, 26261–26275 (2001).
35. Q. Nénon, A. Sicard, P. Kollmann, H. B. Garrett, S. P. A. Sauer, C. Paranicas, A physical model of the proton radiation belts of Jupiter inside Europa's orbit. *J. Geophys. Res.* **123**, 3512–3532 (2018).
36. J. D. Menietti, D. A. Gurnett, J. B. Groene, Radio emission observed by Galileo in the inner Jovian magnetosphere during orbit A-34. *Planet. Space Sci.* **53**, 1234–1242 (2005).

37. O. Santolík, D. A. Gurnett, G. H. Jones, P. Schippers, F. J. Crary, J. S. Leisner, G. B. Hospodarsky, W. S. Kurth, C. T. Russell, M. K. Dougherty, Intense plasma wave emissions associated with Saturn's moon Rhea. *Geophys. Res. Lett.* **38**, L19204 (2011).
38. Y. Y. Shprits, J. D. Menietti, A. Y. Drozdov, R. B. Horne, E. E. Woodfield, J. B. Groene, M. de Soria-Santacruz, T. F. Averkamp, H. Garrett, C. Paranicas, D. A. Gurnett, Strong whistler mode waves observed in the vicinity of Jupiter's moons. *Nat. Commun.* **9**, 3131 (2018).
39. C. C. Chaston, J. W. Bonnell, J. R. Wygant, C. A. Kletzing, G. D. Reeves, A. Gerrard, L. Lanzerotti, C. W. Smith, Extreme ionospheric ion energization and electron heating in Alfvén waves in the storm time inner magnetosphere. *Geophys. Res. Lett.* **42**, 10531–10540 (2015).
40. A. Kotova, E. Roussos, P. Kollmann, N. Krupp, I. Dandouras, Galactic cosmic rays access to the magnetosphere of Saturn. *J. Geophys. Res.* **124**, 166–177 (2019).
41. R. S. Selesnick, D. N. Baker, A. N. Jaynes, X. Li, S. G. Kanekal, M. K. Hudson, B. T. Kress, Observations of the inner radiation belt: CRAND and trapped solar protons. *J. Geophys. Res. Space Phys.* **119**, 6541–6552 (2014).
42. A. E. Doyle, S. J. Desch, E. D. Young, Icy exomoons evidenced by spallogenic nuclides in polluted white dwarfs. *Astrophys. J. Lett.* **907**, L35 (2021).
43. J. A. Miller, R. Ramaty, Ion and relativistic electron acceleration by Alfven and whistler turbulence in solar flares. *Sol. Phys.* **113**, 195–201 (1987).
44. V. Petrosian, Stochastic acceleration by turbulence. *Space Sci. Rev.* **173**, 535–556 (2012).
45. N. Gehrels, "Energetic oxygen and sulfur Ions in the Jovian magnetosphere," thesis, California Institute of Technology, Pasadena, CA (1982).
46. I. Jun, H. Garrett, R. Evans, High-energy trapped particle environments at Jupiter: An update. *IEEE Trans. Nucl. Sci.* **52**, 2281–2286 (2005).
47. H. B. Garrett, M. Kokorowski, S. Kang, R. W. Evans, C. M. S. Cohen, *The Jovian Equatorial Heavy Ion Radiation Environment* (JPL Publication, 2012).
48. C. G. Maclennan, L. J. Lanzerotti, A. Lagg, Hot plasma heavy ion abundance in the inner Jovian magnetosphere (>10 Rj). *Planet. Space Sci.* **49**, 275–282 (2001).
49. P. Kollmann, C. Paranicas, A. Lagg, E. Roussos, Z. H. Lee-Payne, M. Kusterer, D. Smith, N. Krupp, J. Vandegriff, Galileo/EPD user guide, *Earth and Space Science Open Archive* p. 33 (2020).
50. C. M. S. Cohen, E. C. Stone, R. S. Selesnick, Energetic ion observations in the middle Jovian magnetosphere. *J. Geophys. Res.* **106**, 29871–29881 (2001).
51. Z. Lee-Payne, P. Kollmann, M. Grande, T. Knight, Correction of Galileo energetic particle detector, composition measurement system high rate data: Semiconductor dead layer correction. *Space Sci. Rev.* **216**, 5 (2020).
52. J. F. Ziegler, M. D. Ziegler, J. P. Biersack, SRIM—The stopping and range of ions in matter (2010). *Nucl. Instrum. Methods Phys. Res. B* **268**, 1818–1823 (2010).
53. J. E. P. Connerney, S. Kotsiaros, R. J. Oliversen, J. R. Espley, J. L. Joergensen, P. S. Joergensen, J. M. G. Merayo, M. Herceg, J. Bloxham, K. M. Moore, S. J. Bolton, S. M. Levin, A new model of Jupiter's magnetic field from Juno's first nine orbits. *Geophys. Res. Lett.* **45**, 2590–2596 (2018).
54. R. S. Selesnick, Simulation of the anomalous cosmic ray radiation belt with atmospheric production and decay. *Geophys. Res. Lett.* **28**, 3417–3420 (2001).
55. S. Agostinelli, J. Allison, K. Amako, J. Apostolakis, H. Araujo, P. Arce, M. Asai, D. Axen, S. Banerjee, G. Barrand, F. Behner, L. Bellagamba, J. Boudreau, L. Broglia, A. Brunengo, H. Burkhardt, S. Chauvie, J. Chuma, R. Chytracek, G. Cooperman, G. Cosmo, P. Degtyarenko, A. Dell'Acqua, G. Depaola, D. Dietrich, R. Enami, A. Feliciello, C. Ferguson, H. Fesefeldt, G. Folger, F. Foppiano, A. Forti, S. Garelli, S. Giani, R. Giannitrapani, D. Gibin, J. J. Gómez Cadenas, I. González, G. Gracia Abril, G. Greeniaus, W. Greiner, V. Grichine, A. Grossheim, S. Guatelli, P. Gumplinger, R. Hamatsu, K. Hashimoto, H. Hasui, A. Heikkinen, A. Howard, V. Ivanchenko, A. Johnson, F. W. Jones, J. Kallenbach, N. Kanaya, M. Kawabata, Y. Kawabata, M. Kawaguti, S. Kelner, P. Kent, A. Kimura, T. Kodama, R. Kokoulin, M. Kossov, H. Kurashige, E. Lamanna, T. Lampén, V. Lara, V. Lefebure, F. Lei, M. Liendl, W. Lockman, F. Longo, S. Magni, M. Maire, E. Medernach, K. Minamimoto, P. Mora de Freitas, Y. Morita, K. Murakami, M. Nagamatu, R. Nartallo, P. Nieminen, T. Nishimura, K. Ohtsubo, M. Okamura, S. O'Neale, Y. Oohata, K. Paech, J. Perl, A. Pfeiffer, M. G. Pia, F. Ranjard, A. Rybin, S. Sadilov, E. di Salvo, G. Santin, T. Sasaki, N. Savvas, Y. Sawada, S. Scherer, S. Sei, V. Sirotenko, D. Smith, N. Starkov, H. Stoecker, J. Sulkimo, M. Takahata, S. Tanaka, E. Tcherniaev, E. Safai Tehrani, M. Tropeano, P. Truscott, H. Uno, L. Urban, P. Urban, M. Verderi, A. Walkden, W. Wander, H. Weber, J. P. Wellisch, T. Wenaus, D. C. Williams, D. Wright, T. Yamada, H. Yoshida, D. Zschiesche, Geant4—A simulation toolkit. *Nucl. Instrum. Methods Phys. Res. A* **506**, 250–303 (2003).
56. J. A. Burns, M. R. Showalter, D. P. Hamilton, P. D. Nicholson, I. Pater, M. E. Ockert-Bell, P. C. Thomas, The formation of Jupiter's faint rings. *Science* **284**, 1146–1150 (1999).
57. J. D. Anderson, T. V. Johnson, G. Schubert, S. Asmar, R. A. Jacobson, D. Johnston, E. L. Lau, G. Lewis, W. B. Moore, A. Taylor, P. C. Thomas, G. Weinwurm, Amalthea's density is less than that of water. *Science* **308**, 1291–1293 (2005).
58. Q. Nenon, A. Sicard, P. Caron, The rings of Jupiter as seen by the electron and proton radiation belt model Salammbô. *Geophys. Res. Lett.* **45**, 10838–10846 (2018).
59. N. Takato, S. J. Bus, H. Terada, T.-S. Pyo, N. Kobayashi, Detection of a deep 3-μm Absorption feature in the spectrum of Amalthea (JV). *Science* **306**, 2224–2227 (2004).
60. R. S. Selesnick, D. N. Baker, S. G. Kanekal, Proton straggling in thick silicon detectors. *Nucl. Instrum. Methods Phys. Res. B* **394**, 145–152 (2017).

Acknowledgments: We acknowledge support by the PDS through which the HIC data were obtained and R. Wilson (LASP, USA) and R. Selesnick (Air Force Research Laboratory, USA) for assistance in reconstructing the HIC pointing. We are thankful to the GEANT4 collaboration and J. F. Ziegler for making available the GEANT4 and SRIM packages that were used to simulate HIC responses and ring spallation. **Funding:** E.R. and N.K. are supported by the German Space Agency (DLR) through contract 50 QJ 1503 and by the Max Planck Society.
Author contributions: All authors contributed to the discussion and interpretation of the data and the writing of the manuscript. E.R. developed the study concept and performed most data analysis tasks, including simulations of the HIC sensor responses. C.C. contributed to the evaluation and interpretation of the PDS-archived data of HIC. P.K. provided software for the range-energy analysis of HIC responses, generated the processed EPD/CMS data, and performed the magnetic mapping of Galileo measurements. M.P. performed GEANT4 simulations of ring spallation. K.D. contributed to the analysis of HIC and EPD spectra. N.K. and P.G. administered the project on the side of MPS and LIP, respectively. **Competing interests:** The authors declare that they have no competing interests. **Data and materials availability:** All HIC data used in the present study are available through NASA's PDS at https://pds-ppi.igpp.ucla.edu/search/?sc=Galileo&t=Jupiter&i=HIC. Processed Galileo EPD/CMS data are available at sd-www.jhuapl.edu/Galileo_EPD/. The processing steps of these datasets and caveats of the archived datasets are described in Materials and Methods.

Submitted 17 September 2021
Accepted 19 November 2021
Published 12 January 2022
10.1126/sciadv.abm4234